RSC Advances

ROYAL SOCIETY OF CHEMISTRY

PAPER

View Article Online
View Journal | View Issue

Cite this: *RSC Adv.*, 2026, **16**, 15452

Influence of pH-induced particle-size modulation on the electrochemical performance of spinel $ZnFe_2O_4$ anodes for lithium-ion batteries

To Giang Tran, [ab] Thi My Dung Ngo,[c] Anh Huy Phan,[c] Hai Dang Ngo,[c] Ngoc Trung Tran,[c] Hieu Trung Bui,[de] Tuan Loi Nguyen, *[fg] Tran Thi Kieu Ngan,[h] Il Tae Kim *[h] and Quang Hung Nguyen *[fg]

This study synthesizes $ZnFe_2O_4$ spinel *via* a co-precipitation method using $ZnCl_2$ and $Fe(NO_3)_3 \cdot 9H_2O$ as precursors, and the reaction pH is adjusted to 10, 11, and 12 to regulate the particle-size evolution. Based on the thermal analysis of the precursors, the resulting products inform the selection of the optimal calcination temperature for spinel formation (750 °C); the resulting samples are denoted as ZFO_pH 10, ZFO_pH 11, and ZFO_pH 12. Comparative analysis of the pH-regulated samples reveals that pH strongly influences the particle size and key electrochemical properties, including Li^+-storage performance, cycling stability, and electrical conductivity. X-ray diffraction (XRD) analyses confirm that all samples predominantly comprise well-crystallized $ZnFe_2O_4$ without detectable secondary phases within the XRD detection limit. Notably, ZFO_pH 11 exhibits an average particle size of approximately 37 nm, which is considerably smaller than the approximately 42 nm particles observed in ZFO_pH 10. Consequently, the ZFO_pH 11 electrode delivers a high initial charge capacity of 992.78 mAh g^{-1} and maintains a capacity of approximately 910.84 mAh g^{-1} after 60 cycles at 0.1 A g^{-1}. These results demonstrate that pH adjustment is an effective strategy for tuning particle size and crystallinity, thereby enhancing electrochemical performance. Among the synthesized materials, ZFO_pH 11 demonstrates strong potential as an anode material for lithium-ion batteries owing to its favorable combination of particle size, crystallinity, and phase purity.

Received 30th December 2025
Accepted 14th March 2026

DOI: 10.1039/d5ra10094a

rsc.li/rsc-advances

1 Introduction

Among rapidly advancing energy-storage technologies, lithium-ion batteries (LIBs) have become a crucial foundation for applications ranging from portable electronics and computers to large-scale energy systems. However, the anodes of commercial LIBs have nearly reached their developmental limit, making further improvements in electrochemical performance increasingly challenging. Conventional anode materials are primarily based on graphite, which possesses a theoretical capacity of only approximately 372 mAh g^{-1}, considerably lower than those of many emerging materials.[1–3] Additionally, graphite exhibits strong structural anisotropy, numerous surface defects, and a large specific surface area; these characteristics restrict Li^+ insertion into the edge planes during cycling.[4–6] Particularly, the solid electrolyte interphase (SEI) layer tends to form in a nonuniform manner and undergoes repeated rupture and reformation, which continuously consumes the electrolyte and Li^+ ions. This persistent degradation ultimately results in capacity fading and low coulombic efficiency (CE).[6] To mitigate the intrinsic limitations of commercial LIB anodes, a widely adopted strategy is to reduce the particle size of alternative anode materials to the nanoscale. At the nanoscale, materials exhibit enhanced electrode surface area, markedly shortened Li^+-diffusion pathways, and reinforced structural integrity capable of mitigating mechanical stress, which collectively contribute to their outstanding electrochemical performance.[7–9] For example, Ding *et al.* demonstrated that nanosized silicon delivers an impressive capacity of 738 mAh g^{-1} after 200 cycles, substantially higher than that of microsized silicon, which achieves only 249 mAh

[a]*Institute of Research and Development, Duy Tan University, Da Nang City 50000, Vietnam*
[b]*School of Engineering & Technology, Duy Tan University, Da Nang City 50000, Vietnam*
[c]*Faculty of Applied Sciences, Ho Chi Minh City University of Technology and Education (HCMUTE), Thu Duc Ward, Ho Chi Minh City, Vietnam*
[d]*Nguyen Tat Thanh University, Center for Hi-Tech Development, Saigon Hi-Tech Park, Ho Chi Minh City, Vietnam*
[e]*NTT Hi-Tech Institute, Nguyen Tat Thanh University, Ho Chi Minh City, Vietnam*
[f]*Institute of Fundamental and Applied Sciences, Duy Tan University, Ho Chi Minh City 70000, Vietnam. E-mail: nguyentuanloi@duytan.edu.vn; nguyenquanghung5@duytan.edu.vn*
[g]*Faculty of Natural Sciences, Duy Tan University, Da Nang City 50000, Vietnam*
[h]*School of Chemical, Biological & Battery Engineering, Gachon University, Seongnam-si, Gyeonggi-do, 13120, Republic of Korea. E-mail: itkim@gachon.ac.kr*

g^{-1}.[10] Similarly, Hu *et al.* synthesized spinel $CoMn_2O_4$, exhibiting a high capacity of 624 mAh g^{-1} and retaining 75.5% of its initial capacity at a current density of 0.2 A g^{-1} after 50 cycles.[11]

Among the various materials investigated for LIB anodes, $ZnFe_2O_4$ stands out as a highly promising candidate due to the synergistic combination of its intrinsic material properties and unique Li^+ storage mechanisms.[12,13] $ZnFe_2O_4$ is not only derived from naturally abundant resources but also possesses a high theoretical capacity of 1072 mAh g^{-1}, which is superior to that of other spinel-structured oxides and significantly exceeds that of commercial graphite.[12–14] Structurally, Zn-ferrite crystallizes in the spinel structure with the general formula AB_2O_4, where A is a divalent cation and B is a trivalent cation, and possesses a cubic close-packed arrangement of O^{2-} anions.[15–17] Within this structure, B-site cations occupy half of the octahedral sites (16d), A-site cations reside in one-eighth of the tetrahedral sites (8a), and the remaining octahedral sites (16c) remain vacant.[16] Therefore, these unoccupied 16c positions enable Li^+ ions to hop from one tetrahedral (8a) site to another through a three-dimensional (3D) diffusion network spanning the *x*, *y*, and *z* directions, offering faster transport pathways compared with materials constrained by 2D frameworks.[18,19] Additionally, this robust 3D ion-diffusion channel offers significant advantages for anode performance, including enhanced Li^+ mobility, host-lattice structural stability, and enhanced electrochemical efficiency.[16,20] For example, Wang *et al.* reported that spinel-type materials preserve approximately 75% and 58% of their original capacity at 5C and 10C, respectively.[21] Another stricking point is that at the nanoscale, $ZnFe_2O_4$ exhibits flexible cation distribution between tetrahedral (A) and octahedral (B) sites, typically expressed as $[(Zn^{2+})_{1-x}(Fe^{3+})_x]_A[(Zn^{2+})_x(Fe^{3+})_{2-x}]_B(O^{2-})_4$.[12,22] This indicates that portions of Zn^{2+} and Fe^{3+} ions reside in both A and B sites, generating additional electrochemically active centers and enhancing the chemical stability of $ZnFe_2O_4$.[12] Moreover, $ZnFe_2O_4$ undergoes a combination of conversion and alloying reactions.[23] Upon lithiation, Zn^{2+} and Fe^{3+} ions are reduced to metallic Zn and Fe, accompanied by the formation of Li_2O (eqn (1)). Subsequently, metallic Zn further reacts with Li^+ to generate Li–Zn alloys (eqn (2)).[24]

$$ZnFe_2O_4 + 8Li^+ + 8e^- \rightarrow Zn + 2Fe + 4Li_2O \quad (1)$$

$$Zn + Li^+ + e^- \rightarrow LiZn \quad (2)$$

The alloying reaction between Li^+ and Zn considerably contributes to the reversible electrochemical behavior and introduces additional Li^+ storage sites, enabling $ZnFe_2O_4$ to surpass the capacity limit typically constrained by conventional conversion mechanisms.[14,23] Owing to these benefits, numerous studies have reported impressive electrochemical results. For example, Jia *et al.* synthesized nanosized $ZnFe_2O_4$ coated with carbon using ionic-liquid-assisted synthesis, achieving a stable capacity of 1091 mAh g^{-1} after 190 cycles at 1C, and retaining a capacity of 216 mAh g^{-1} even at 20C.[25] Similarly, Yue *et al.* prepared $ZnFe_2O_4$/PDA composites and showed that an 8 nm PDA coating yielded the best electrochemical performance, with an initial discharge capacity of 2079 mAh g^{-1} at 1 A g^{-1}.[24] Additionally, Yao *et al.* prepared $ZnFe_2O_4$/graphite composites synthesized *via* hydrothermal methods that demonstrated a remarkable capacity of 1450 mAh g^{-1} after 150 cycles at 0.1 A g^{-1} for nanoparticles sized 20–30 nm.[26] Motivated by the promising characteristics of spinel $ZnFe_2O_4$, the present study aims to synthesize $ZnFe_2O_4$ *via* a simple co-precipitation approach, enabling precise control over the nanoparticle size through pH adjustment (pH 10, 11, and 12). This strategy enables the systematic evaluation of the electrochemical properties of $ZnFe_2O_4$ and provides insights into how the pH-dependent particle size influences the overall performance of the $ZnFe_2O_4$ anode material.

2 Materials and methods

2.1 Synthesis of $ZnFe_2O_4$ materials

The precursors used for the co-precipitation synthesis included zinc chloride ($ZnCl_2$), iron(III) nitrate nonahydrate ($Fe(NO_3)_3 \cdot 9H_2O$), and sodium hydroxide (NaOH), supplied by Xylong Co. (China). First, $ZnCl_2$ (0.681 g) and $Fe(NO_3)_3 \cdot 9H_2O$ (4.039 g) were dissolved in 50 mL of deionized water, maintaining a Zn : Fe molar ratio of 1 : 2. Subsequently, the resulting solution was slowly added dropwise into a three-necked flask containing 200 mL of deionized water preheated to 95 °C and magnetically stirred for 10 min to enhance reaction kinetics and minimize localized supersaturation. Next, the mixture was cooled naturally to room temperature. Once it reached 25 °C, NaOH solution was gradually introduced to induce the precipitation of Zn^{2+} and Fe^{3+} ions while precisely controlling the NaOH addition to achieve the desired pH values of 10, 11, and 12. The suspension was continuously stirred for an additional hour to ensure homogeneous particle formation. Subsequently, the resulting precipitates were washed several times with deionized water and ethanol by centrifugation at 4500 rpm for 5 min to remove residual ions and impurities. In the subsequent calcination step, the samples corresponding to the three pH conditions were annealed at 750 °C for 3 h in air to convert the precursors into metal-oxide phases. Finally, the obtained oxides were ground into fine powders and designated as ZFO_pH 10, ZFO_pH 11, and ZFO_pH 12.

2.2 Material characterization

The structural and morphological characteristics of the powders synthesized at the three pH values were examined using advanced characterization techniques. Thermogravimetric analysis (TGA) was conducted to evaluate the thermal stability and decomposition behavior of the as-prepared precursors before calcination. The TGA results provide insight into the removal of absorbed water, residual nitrates, and other volatile species, allowing optimization of the annealing temperature required to obtain phase-pure $ZnFe_2O_4$. Second, X-ray diffraction (XRD) was employed to identify the crystal structure of the spinel ferrite phase and detect any undesirable secondary phases in the synthesized samples, thereby evaluating their potential influence on the material properties. Scanning electron microscopy (SEM) was used to observe the particle distribution and surface morphology, which play

crucial roles in assessing the electrochemical performance of the material. In addition, transmission electron microscopy (TEM) was utilized to provide a more detailed investigation of the internal microstructure and precise nanoscale dimensions. Energy-dispersive X-ray spectroscopy (EDS) was then used to determine the components and proportions of elements in the synthesized samples. Finally, X-ray photoelectron spectroscopy (XPS) was conducted to investigate the surface chemical composition and the specific oxidation states of the constituent elements, thereby elucidating the effect of pH on the chemical bonding of the materials.

2.3 Electrochemical measurements

The as-prepared ZFO powders were mixed with Super P and poly(acrylic acid) in a weight ratio of 70 : 15 : 15 and dispersed in ethanol to form a homogeneous slurry. Subsequently, the slurry was stirred overnight to ensure homogeneity before being coated onto a copper foil using the doctor-blade technique to form uniform electrode films. The coated copper foils were then dried in a vacuum oven at 75 °C for 3 h to remove residual solvents and moisture. The dried electrode films were then punched into circular disks with a diameter of 1.5 cm, yielding an active material loading of 1.2–1.3 mg cm^{-2}, and subsequently assembled into coin-type cells (CR_2032, with a diameter of 20 mm and a thickness of 3.2 mm).

The coin-cell configuration (Fig. S1) consisted of a ZFO-based anode, a Celgard 2400 polymer separator, and an electrolyte composed of 1 M lithium hexafluorophosphate dissolved in a 1 : 1 volume ratio mixture of diethyl carbonate and ethylene carbonate. Metallic lithium was used as both the counter and reference electrodes. Cyclic voltammetry (CV) was conducted in the potential window of 0.01–3.00 V (*vs.* Li/Li^+) to investigate the redox reactions occurring in the spinel $ZnFe_2O_4$. Additionally, galvanostatic charge–discharge cycling was performed in the same voltage range at a current density of 0.1 A g^{-1} to evaluate the specific charge–discharge capacities. The charge-storage kinetics were further analyzed by varying the scan rates from 0.3 mV s^{-1} to 1.2 mV s^{-1}. Finally, electrochemical impedance spectroscopy (EIS) measurements were performed using a Gamry 1010E system in the frequency range from 10^6 Hz to 0.1 Hz, with an AC perturbation amplitude of 10 mV, under open-circuit voltage conditions at room temperature to examine the impedance characteristics of the ZFO anodes.

3 Results and discussion

In this research, the ZFO material was successfully synthesized using two salts, $ZnCl_2$ and $Fe(NO_3)_3$, *via* the co-precipitation method at pH 10, 11, and 12, followed by high-temperature calcination at 750 °C. The mechanism for $ZnFe_2O_4$ phase formation is as follows. First, the co-precipitation of metal ions with NaOH forms hydroxides (eqn (3) and (4)). High-temperature calcination converts these hydroxides into metal oxides (eqn (5) and (6)). Finally, the reaction between zinc oxide and iron oxide produces $ZnFe_2O_4$ (eqn (7)).

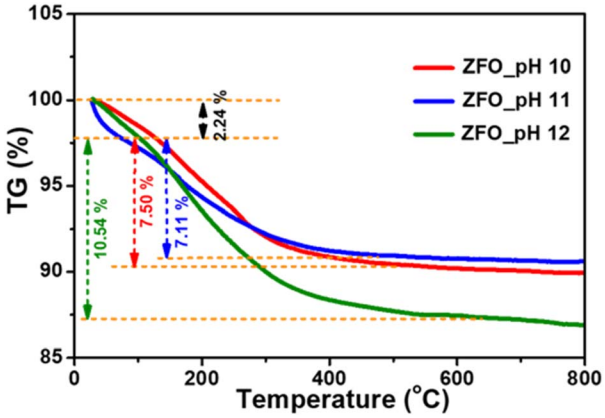

Fig. 1 TGA curve of the as-synthesized $ZnFe_2O_4$ precursor (pH 10, pH 11, and pH 12).

$$ZnCl_2 + 2NaOH \rightarrow Zn(OH)_2 \downarrow + 2NaCl \quad (3)$$

$$Fe(NO_3)_3 + 3NaOH \rightarrow Fe(OH)_3 \downarrow + 3NaNO_3 \quad (4)$$

$$Zn(OH)_2 \rightarrow ZnO + H_2O \quad (5)$$

$$2Fe(OH)_3 \rightarrow Fe_2O_3 + 3H_2O \quad (6)$$

$$ZnO + Fe_2O_3 \rightarrow ZnFe_2O_4 \quad (7)$$

Fig. 1 shows that the post-synthesis material undergoes three characteristic mass-loss stages when heated to 800 °C under air. In the first stage (under 150 °C), all three samples lose approximately 2.24% of their mass, corresponding to the removal of residual water and solvent left after the centrifugation process.[27,28] In the second phase, ranging from 200 to 450 °C, the ZFO_pH 10 and pH 11 samples exhibit comparable mass losses of approximately 7.50% and 7.11%, respectively, whereas the ZFO_pH 12 sample displays a distinctly higher mass loss of approximately 10.54%. This mass loss at this temperature is attributed to the gradual decomposition of metal hydroxides ($Zn(OH)_2$ and $Fe(OH)_3$) and residual nitrate species into ZnO and Fe_2O_3, which subsequently promote the formation of the $ZnFe_2O_4$ spinel phase.[28–30] Additionally, the increased mass loss of ZFO_pH 12 is attributed to the high concentration of hydroxyl ions in the high-pH synthesis environment. In other words, the abundance of OH^- groups not only promoted extensive dehydroxylation reactions but also facilitated the formation of a gelatinous precipitate structure that traps water molecules, which are subsequently released only at elevated temperatures.[31,32] Importantly, this difference in mass loss for ZFO_pH 12 does not compromise the quality of the final product when the mass curves of the three samples begin to stabilize above approximately 500 °C, indicating the initial formation of the spinel phase. Additionally, above 600 °C, the TGA curve becomes nearly horizontal at approximately 87–90% of its initial mass, demonstrating that the material has reached thermal stability. Moreover, the total mass loss of around 10–13% suggests that the obtained product possesses high purity with minimal remaining organic species or hydroxyl groups.[33]

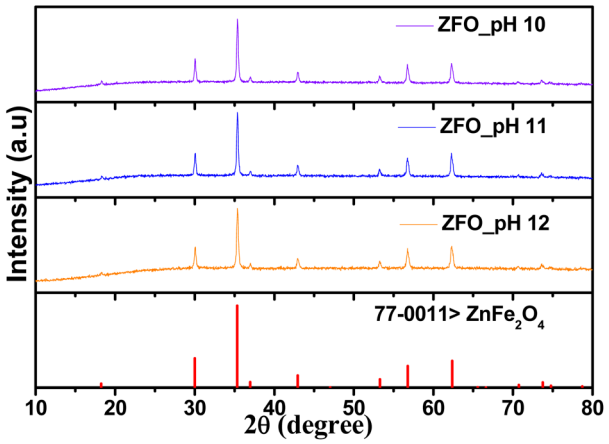

Fig. 2 XRD patterns of ZFO_pH 10, ZFO_pH 11, and ZFO_pH 12 samples and standard peaks of $ZnFe_2O_4$.

Based on these TGA results, it is evident that a calcination temperature of approximately 750 °C is optimal for all samples. This temperature ensures the complete removal of organic residues and adsorbed moisture and promotes the full solid-state reaction between ZnO and Fe_2O_3. This leads to the formation of well-developed spinel $ZnFe_2O_4$ particles with an optimal crystallite size, which is beneficial for enhancing the electrochemical performance of the anode.[34] In contrast, calcination at excessively high temperatures may induce grain overgrowth, which increases the risk of mechanical stress during Li^+ insertion/extraction, reduces the active surface area, and hinders ion-diffusion pathways. These factors collectively resulted in a considerable decline in the capacity of the electrode.[35,36]

Fig. 2 shows the XRD patterns of the ZFO_pH 10, ZFO_pH 11, and ZFO_pH 12 samples, along with the standard $ZnFe_2O_4$ pattern. All three ZFO samples synthesized at pH 10, 11, and 12 exhibit the characteristic diffraction peaks of $ZnFe_2O_4$ (77-0011). The prominent peaks at 30.0°, 35.3°, 42.9°, 56.7°, and 62.3° correspond to the (220), (311), (400), (511), and (440) crystal planes, respectively.[37,38] The peak positions perfectly match those of the ZFO samples synthesized at pH 10, 11, and 12, indicating that the products are nearly single-phase, with negligible or very low-intensity impurities or amorphous peaks. This confirms that the co-precipitation process followed by calcination at 750 °C for 3 h effectively produces high-purity $ZnFe_2O_4$.

The surface morphology of the $ZnFe_2O_4$ samples synthesized at different pH values was first examined by SEM, as shown in Fig. S2. The observations indicate that at pH 10, the sample consists of nanoparticles but exhibits considerable agglomeration. Increasing the pH to 11 results in significantly improved dispersion with a homogeneous surface, suggesting that nucleation was well-controlled and crystallinity was enhanced at this concentration. In contrast, the ZFO_pH 12 sample displays a strong tendency for nanoparticles to aggregate into large, dense clusters. To accurately determine the particle size and overcome the resolution limits of SEM, TEM analysis was performed (Fig. S3). The statistical size distribution measured from over 100 particles reveals that the average particle sizes are 42.39 ± 1.88 nm for ZFO_pH 10, 37.25 ± 1.26 nm for ZFO_pH 11, and 33.64 ± 0.62 nm for ZFO_pH 12. Notably, while the SEM images initially suggested that ZFO_pH 12 comprised larger particles, the TEM analysis clarifies that this sample actually possesses the smallest primary crystallite size, approximately 33 nm, but suffers from the most severe agglomeration. This phenomenon indicates that the high pH environment not only accelerates the nucleation rate (resulting in smaller primary particles) but also promotes the formation of dense aggregates due to the abundance of hydroxyl groups.[39,40] Consequently, ZFO_pH 11 is identified as the optimal sample, striking a balance between a small crystallite size and uniform dispersion without significant agglomeration. This structural feature is expected to maximize the effective specific surface area, thereby enhancing the electrochemical performance of the electrode.[41,42]

Fig. 3 shows elemental-distribution maps (EDS mapping) of the $ZnFe_2O_4$ sample. The results show that the three main constituent elements, Zn, Fe, and O, are uniformly distributed across the entire surface of the sample with relatively consistent signal intensities. This indicates that the synthesis process successfully produced a spinel $ZnFe_2O_4$ phase with a homogeneous dispersion of Zn^{2+} and Fe^{3+} cations. Quantitative EDS analysis (Table S1) further reveals that the Fe/Zn atomic ratio ranges from 2.11 to 2.39, which is reasonably close to the theoretical value for $ZnFe_2O_4$ (Fe/Zn = 2). Overall, the EDS mapping shows a uniform distribution of Zn, Fe, and O, and the elemental ratios approach the theoretical values, thereby confirming the formation of high-purity $ZnFe_2O_4$ spinel. The experimental Fe/Zn ratio (2.11–2.39) is consistently higher than the theoretical ratio (2.00). This indicates that the synthesized $ZnFe_2O_4$ material is either iron-rich or zinc-deficient. This type of nonstoichiometric defect likely results in the substitution of Fe^{3+} at Zn^{2+} tetrahedral sites, creating a partially inverse spinel structure. The electrical conductivity of $ZnFe_2O_4$ spinel oxides primarily relies on electron hopping between Fe^{3+} and Fe^{2+} ions. Although all samples are Fe-rich (Fe/Zn > 2.00), a defect known to enhance conductivity, the ZFO_pH 11 sample is predicted to exhibit the best overall electrical conductivity. This is due to the

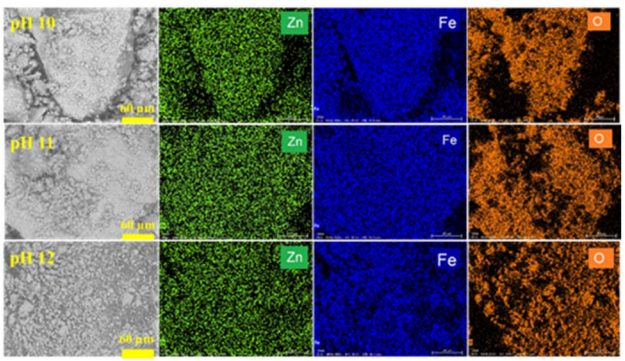

Fig. 3 EDS-mapping images of $ZnFe_2O_4$ synthesized at pH 10, pH 11, and pH 12.

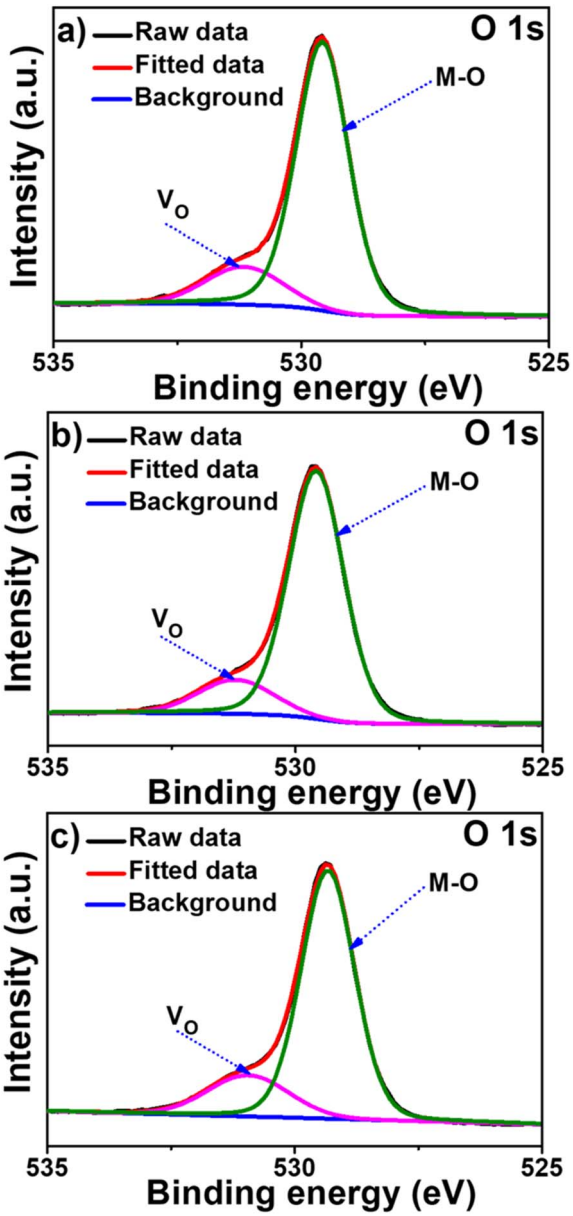

Fig. 4 High-resolution XPS spectra of O 1s for the synthesized samples (a) ZFO_pH 10, (b) ZFO_pH 11, and (c) ZFO_pH 12.

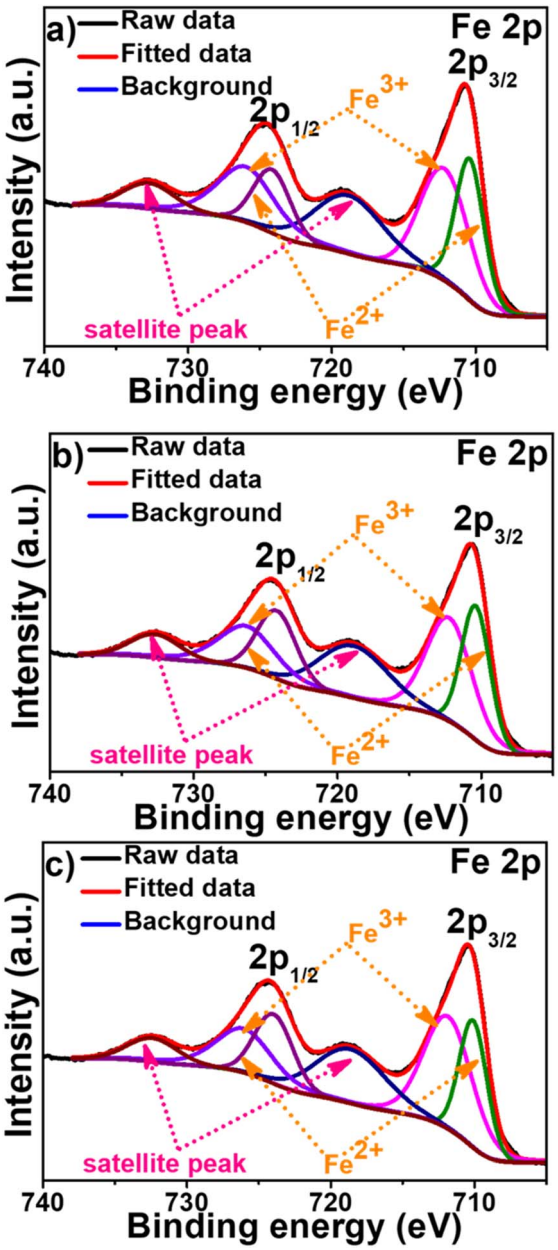

Fig. 5 High-resolution XPS spectra of Fe 2p for the synthesized samples (a) ZFO_pH 10, (b) ZFO_pH 11, and (c) ZFO_pH 12.

combination of the smallest nanoparticle size (37 nm) and highest uniformity, which maximizes the specific surface area and shortens the electron/ion diffusion pathways, leading to improved electrochemical performance. Other samples, whether more Fe-rich at pH 10 or less Fe-rich at pH 12, are hindered by larger sizes and/or higher agglomeration.

The surface chemical bonding states of the three $ZnFe_2O_4$ samples synthesized at pH 10, 11, and 12 were analyzed using XPS and results were presented in Fig. S4. Fig. S5 shows the peaks at around 1021, 1044 eV corresponding to Zn $2p_{3/2}$ and Zn $2p_{1/2}$, respectively.[43,44] A slight decrease in Zn 2p binding energy was observed with increasing overall pH (Fig. S5), suggesting a subtle change in the local electronic environment of the Zn^{2+} ions. This change may be related to altered cation distribution and oxygen defect concentration within the spinel crystal lattice.

Fig. 4a–c reveals that the O 1s spectra of all three samples can be deconvoluted into two characteristic peaks: the M–O peak (at approximately 529.5 eV), representing lattice oxygen bonded to metal ions, and the V_O peak (at approximately 531.1 eV), corresponding to oxygen vacancies.[42] The dominance of the M–O peak demonstrates the high crystallinity of all synthesized samples. The influence of the synthesis pH is further corroborated by the high-resolution Fe 2p XPS spectra as shown in Fig. 5a–c. The spectra exhibit a characteristic spin–orbit splitting into $2p_{3/2}$ and $2p_{1/2}$ regions, accompanied by satellite peaks. The deconvolution of the main 2p peak confirms the

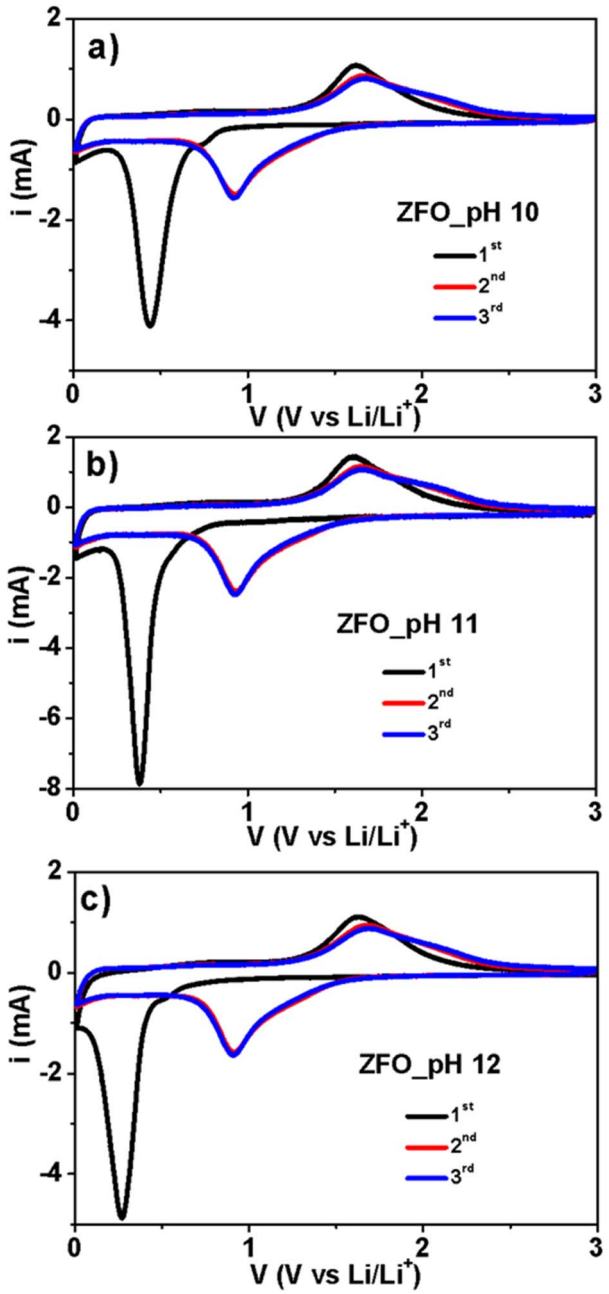

Fig. 6 Cyclic voltammetry profiles of electrodes synthesized at (a) pH 10, (b) pH 11, and (c) pH 12.

coexistence of two oxidation states: Fe^{3+} and Fe^{2+} in the samples.[45] The ratio between Fe^{3+} and Fe^{2+}, between V_O and M–O in the samples was calculated from XPS analysis and shown in Table S2.

It is interesting that these ratios (Fe^{3+}/Fe^{2+}, V_O/M–O) in the ZFO_pH 11 sample are lowest compared to ZFO_pH 10 and ZFO_pH 12 samples, revealing the stable spinel structure with low defects. In addition, the presence of both Fe^{3+} and Fe^{2+} with comparable amounts in the materials provides ideal conditions for the electron hopping mechanism. This phenomenon significantly minimizes the charge-transfer resistance and enhances the electrochemical reaction kinetics of the electrode materials.[46,47] This structural optimization fundamentally explains the superior capacity of the ZFO_pH 11 electrode.

In this study, the electrochemical behavior of ZFO materials was investigated using CV. The CV curves were recorded in the voltage range of 0.01–3.00 V at a scan rate of 0.3 mV s^{-1}, as shown in Fig. 6a–c, to monitor the lithium insertion and extraction processes occurring at the electrode. The CV profiles of ZFO samples synthesized at different pH values all exhibit a strong cathodic peak in the first cycle at low potentials, located at approximately 0.44 V (pH 10), 0.37 V (pH 11), and 0.27 V (pH 12). These peaks correspond to the initial lithiation of $ZnFe_2O_4$, including the irreversible reduction of Fe^{3+} to Fe^0 and Zn^{2+} to Zn^0, formation of Li_2O (eqn (8)–(10)), alloying of Li–Zn (eqn (11)), and concurrent decomposition of the electrolyte forming the SEI.[48,49] From the second cycle onward, the SEI layer is fully formed and stabilized. This causes the initial low-potential reduction peak to disappear and shift to a higher potential, producing a stable cathodic peak at approximately 0.93 V. This peak reflects the reversible reduction of the converted ZnO and Fe_2O_3 phases to metallic Zn and Fe, respectively, indicating a more stable conversion-type Li-storage mechanism in subsequent cycles. During the first anodic scan, a prominent oxidation peak is observed at approximately 1.66 V, which shifts slightly to approximately 1.69 V from the second cycle onward. This feature corresponds to the reverse oxidation of the metallic phases formed during the initial reduction process, including the oxidation of Fe^0 to Fe^{3+} and Zn^0 to Zn^{2+} (eqn (12) and (13)).[24,50] From the second cycle onward, the cathodic and anodic peaks nearly overlap, indicating that the redox reactions proceed stably and are highly reversible. This overlap demonstrates the high reversibility and excellent cycling stability of the $ZnFe_2O_4$ electrode during Li^+ insertion and extraction.

$$ZnFe_2O_4 + xLi^+ + xe^- \rightarrow Li_xZnFe_2O_4 \quad (8)$$

$$Li_xZnFe_2O_4 + yLi^+ + ye^- \rightarrow Li_{x+y}ZnFe_2O_4 \quad (9)$$

$$Li_{x+y}ZnFe_2O_4 + zLi^+ + ze^- \rightarrow 2Fe + Zn + uLi_2O \quad (10)$$

$$Zn + Li^+ + e^- \rightarrow LiZn \quad (11)$$

$$2Fe + 3Li_2O \rightarrow 6Li^+ + 6e^- + Fe_2O_3 \quad (12)$$

$$Zn + Li_2O \rightarrow 2Li^+ + 2e^- + ZnO \quad (13)$$

The charge–discharge profiles of the ZFO anodes recorded within the operating voltage window of 0.01–3 V, are depicted in Fig. 7a–c. Among the three samples, ZFO_pH 11 exhibits the highest initial discharge capacity, reaching 1323.28 mAh g^{-1}, whereas ZFO_pH 10 and ZFO_pH 12 exhibit comparatively lower capacities of 1053.16 mAh g^{-1} and 1216.91 mAh g^{-1}, respectively. Notably, all three measured capacities surpass the theoretical capacity of $ZnFe_2O_4$ (approximately 1000 mAh g^{-1}).[51] All three electrodes reach only approximately 70% of the initial coulombic efficiency (ICE) in the first charge–discharge cycle. This substantial loss is primarily attributed to the irreversible consumption of Li^+ during SEI formation on the electrode

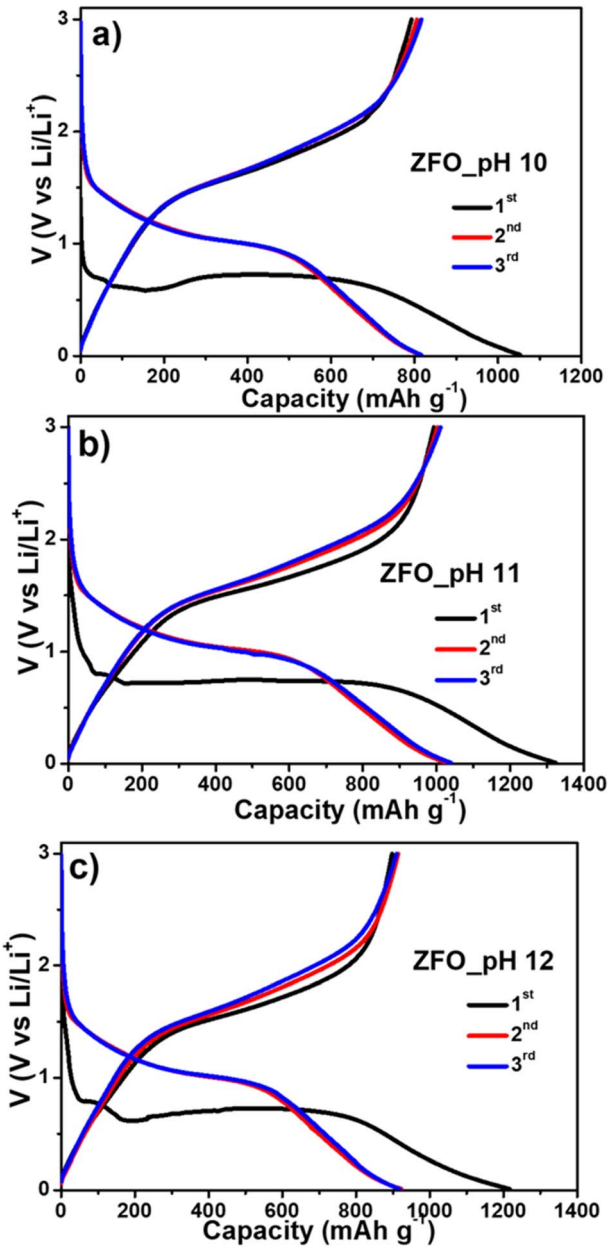

Fig. 7 Voltage profiles of (a) ZFO_pH 10, (b) ZFO_pH 11, and (c) ZFO_pH 12 electrodes.

surface, which results from parasitic reactions between the electrode and electrolyte.[52,53] Furthermore, part of the Li^+ becomes trapped in conversion products such as Li_2O or immobilized at surface defect sites. This prevents its recovery during subsequent charging, thereby further decreasing the ICE in the first cycle.[53,54] Once the SEI layer stabilizes, the CE of all samples rapidly increases to nearly 100% in the second cycle. This improvement is attributed to the protective role of the SEI, which blocks direct electron transfer to the electrolyte and consequently suppresses parasitic side reactions.[52,55] Consequently, further Li^+ loss becomes negligible, allowing the electrodes to operate stably over subsequent cycles. This phenomenon is evident in Fig. 7, where the voltage profiles of the second and third cycles nearly overlap, indicating highly reversible lithiation/delithiation and excellent cycling reproducibility.

From a theoretical perspective, regulating the nanoparticle size *via* pH adjustment is anticipated to enhance the electrochemical performance of spinel ferrites by expanding the active surface area, shortening the Li^+-diffusion pathways, improving the high-rate capability, and mitigating the internal strain during cycling.[56–60] However, the ZFO_pH 12 electrode consistently delivers lower discharge capacities than ZFO_pH 11 across all three cycles. This performance degradation can be attributed to the formation of soluble zinc-hydroxo complexes under highly alkaline conditions. At an elevated pH, Zn^{2+} tends to form species such as $[Zn(OH)_4]^{2-}$, $Zn(OH)^{3-}$, and $Zn(OH)_2$, which preferentially remain dissolved rather than precipitating.[61] Therefore, the Zn : Fe ratio in the ZFO_pH 12 precipitate deviates from the stoichiometry of ideal $ZnFe_2O_4$, weakening the lithium-storage capability of the material compared with ZFO_pH 11.[51] Additionally, previous studies report that excessively high pH accelerates nucleation and crystal growth, leading to oversized crystallites with poor electrochemical activity or electronically perturbed structures owing to continuous cation inversion between Fe^{3+} and Zn^{2+}.[37] Particularly, the highly crystalline nature of ZFO_pH 12 also tends to produce a brittle framework that accumulates mechanical stress during lithiation/delithiation, which explains the noticeable capacity decay in later cycles.[62,63] In terms of the ZFO_pH 10 electrode, the lower OH^- concentration decreases the supersaturation level, thereby suppressing nucleation. Therefore, with fewer nuclei formed, the remaining Zn^{2+} and Fe^{3+} ions are preferentially deposited onto existing seeds and accelerate crystal growth, ultimately producing larger particles.[64,65] Consequently, the enlarged particle size limits the electrochemical activity, similar to that observed in the ZFO_pH 12 electrode. In contrast, ZFO_pH 11 attains an optimal balance between the nucleation and crystal-growth rates. As evidenced by the TEM images in Fig. S3, ZFO_pH 11 exhibits smaller and more uniform particle sizes than the other two electrodes, thereby providing a larger active surface area and shorter Li^+-diffusion pathways. Consequently, ZFO_pH 11 exhibits the highest discharge capacity and best electrochemical performance among the three samples across all the measured cycles.[51]

The cycling performance of the ZFO electrodes was evaluated *via* repeated charge–discharge measurements at a current density of 0.1 A g^{-1}, while monitoring the corresponding CE, as shown in Fig. 8a. The first-cycle charge capacity of the ZFO_pH 10 electrode is approximately 792.8 mAh g^{-1}. During the initial stage, the capacity increases slightly and remains relatively stable. However, from approximately the 37th cycle onward, the capacity begins to decline noticeably and continues to decrease in subsequent cycles. After 60 cycles, the remaining capacity is approximately 686.8 mAh g^{-1}, corresponding to a capacity retention of approximately 86.6%, indicating a moderate cycling stability. Conversely, the ZFO_pH 11 sample exhibits the highest initial charge capacity of approximately 992.7 mAh g^{-1}. Although the capacity slightly decreases from approximately the 5th cycle, it remains stable throughout the measurement. After

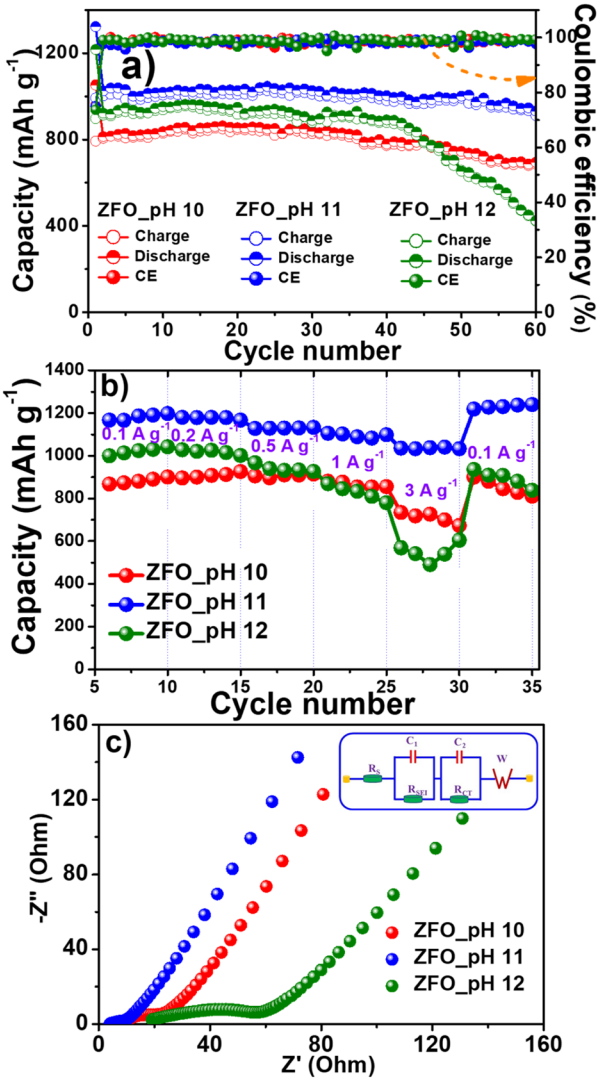

Fig. 8 (a) Cycling behavior, (b) rate capability, and (c) EIS results of ZFO electrodes prepared at various pH values.

60 cycles, the electrode retains approximately 910.84 mAh g^{-1}, corresponding to a retention of approximately 91.8%, thereby demonstrating superior cycling stability compared to the other samples. In contrast, ZFO_pH 12 shows an initial capacity of approximately 897.7 mAh g^{-1}, which remains relatively stable in the early cycles. However, from approximately the 42nd cycle, the capacity decreases rapidly, indicating poor stability during repeated charge–discharge cycles. At the end of 60 cycles, the remaining capacity is only approximately 424.6 mAh g^{-1}, corresponding to a retention of 47.3%, which reflects significant degradation owing to the unstable electrode structure. The electrochemical properties indicate that the ZFO_pH 11 electrode exhibits superior performance compared with the other samples. After the first cycle, the CE of all electrodes quickly increases and remains stable at approximately 100% in subsequent cycles, indicating excellent reversibility of the charge–discharge process. The high CE stability also suggests a robust electrode structure with minimal side reactions during long-term operation. Moreover, compared to previously reported Zn- and Fe-based anode materials (Table S3), the ZFO_pH 11 electrode demonstrates a competitive electrochemical performance, particularly in terms of capacity retention and stable CE, highlighting its potential application as an LIB anode.

Fig. 8b presents the rate capability of the ZFO electrodes synthesized at different pH values through charge–discharge measurements at increasing current densities from 0.1 to 3 A g^{-1}. In general, the capacity of all samples decreased with increasing current density, reflecting the typical kinetic behavior of transition-metal-based anode materials. For ZFO_pH 10, as the current density increases from 0.1 to 0.2, 0.5, 1, and 3 A g^{-1}, the charge capacities decrease to 900.8, 925.9, 914.5, 855.4, and 673.1 mAh g^{-1}, respectively, indicating moderate capacity retention under high-current conditions. Despite the significant capacity decay at high current densities, the electrode shows good recovery when the current returns to its initial value. ZFO_pH 11 exhibits a superior rate performance compared with the other samples. As the current density increases, the capacity remains high, reaching 1198.1, 1167.6, 1133.7, 1098.9, and 1033.0 mAh g^{-1} at current densities of 0.1, 0.2, 0.5, 1, and 3 A g^{-1}, respectively. This indicates efficient electron transport and Li^+-ion diffusion, enabling a stable electrode performance even under high-current conditions. In contrast, ZFO_pH 12 displays a more pronounced capacity decay with increasing current density, with capacities of 1042.6, 1002.0, 927.2, 779.5, and 604.7 mAh g^{-1}, revealing kinetic limitations and structural instability under high-current operation. Notably, even at a current density of 3 A g^{-1}, the electrodes retain a significant fraction of their initial capacities. Specifically, ZFO_pH 10 retains approximately 74.7% of its initial capacity, ZFO_pH 11 exhibits the highest retention of approximately 86.2%, and ZFO_pH 12 only retains approximately 58%, indicating inferior high-rate capabilities. When the current density returns to 0.1 A g^{-1}, all electrodes show nearly full capacity recovery. The recovered capacities of ZFO_pH 10, ZFO_pH 11, and ZFO_pH 12 are 810.3, 1240.8, and 838.1 mAh g^{-1}, respectively, demonstrating good reversibility of the charge–discharge process and structural robustness of the electrodes over a wide range of current densities. Among them, ZFO_pH 11 continues to show a clear advantage in capacity recovery, further confirming its potential for LIB applications requiring fast charge–discharge capability.

The EIS results of the ZFO electrodes synthesized at different pH values are shown in Fig. 8c, and the corresponding fitted resistance parameters are summarized in Table S4. In the Nyquist plots, each spectrum features a semicircle in the medium-frequency region, representing the impedance associated with SEI-layer formation and charge transfer at the electrode/electrolyte interface, along with a sloped line in the low-frequency region related to Li^+-ion diffusion within the bulk material.[51] The similar overall shapes of the EIS spectra indicate that all electrodes follow the same electrochemical mechanism; however, pronounced differences in the semicircle diameters reflect variations in reaction kinetics. As listed in Table S4, the solution resistance (R_S) and SEI-related resistance (R_{SEI}) of ZFO_pH 11 are slightly lower than those of ZFO_pH 10 and significantly lower than those of ZFO_pH 12, indicating

improved electrolyte contact and a more stable SEI layer for the pH 11 sample. In contrast, the larger R_S and R_{SEI} values observed for ZFO_pH 12 suggest inferior interfacial properties, likely associated with stronger particle agglomeration and a less homogeneous electrode surface. More importantly, the charge-transfer resistance (R_{CT}) values of ZFO_pH 10, ZFO_pH 11, and ZFO_pH 12 are 6.98 Ω, 3.54 Ω, and 18.75 Ω, respectively. ZFO_pH 11 exhibits the lowest R_{CT}, indicating that electron transfer at the electrode/electrolyte interface proceeds significantly more efficiently. This suggests that the electrode structure of the pH 11 sample facilitates effective charge transport, thereby enhancing the electrochemical reaction kinetics, particularly under high-current-density conditions. In contrast, ZFO_pH 12 shows the highest R_{CT}, reflecting a substantial hindrance to charge-transfer processes. Although ZFO_pH 12 exhibits particle size comparable to that of ZFO_pH 10, the significantly enlarged semicircle indicates that the impedance difference is not governed solely by morphology. At the molecular scale, synthesis under strong alkaline conditions (pH 12) may induce surface hydroxylation or local cation disorder, which can disrupt electronic pathways and increase the interfacial charge-transfer barrier, resulting in higher R_{CT}. Such a high impedance may limit the high-rate capability of the electrode, leading to pronounced capacity fading at elevated current densities. This is consistent with the previously discussed rate capability (Fig. 8b) and cycling stability results (Fig. 8a). ZFO_pH 10 exhibits an intermediate R_{CT}, indicating a relatively good charge-transfer ability, although it is still inferior to that of ZFO_pH 11. Overall, ZFO_pH 11 plays a key role in maintaining a stable capacity and high-rate performance during repeated charge–discharge cycling. These findings are consistent with the rate-capability and cycling-performance analyses, confirming that optimizing the synthesis at pH 11 produces an electrode structure favorable for both electron conduction and Li^+-ion diffusion.

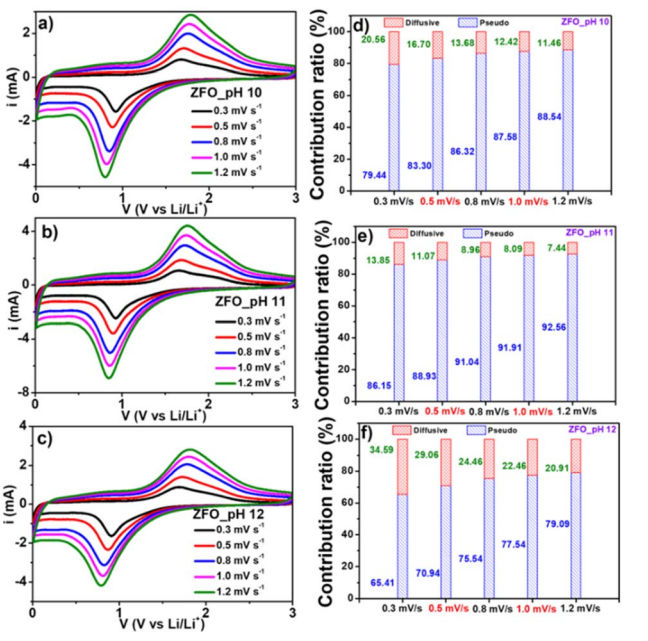

Fig. 9 (a–c) CV profiles and (d–f) diffusive and pseudo contribution ratios for the ZFO_pH 10, ZFO_pH 11, and ZFO_pH 12 electrodes at different scan rates.

Fig. 9a–c illustrates the evolution of the CV curves of the three ZFO electrodes (ZFO_pH 10, ZFO_pH 11, and ZFO_pH 12), whereas Fig. 9d–f depicts their charge-storage kinetics as the scan rate progressively increases from 0.3 to 1.2 mV s^{-1}. Across all five scan rates, the redox peak currents exhibit a proportional relationship with the scan rate for both the anodic and cathodic processes, corresponding to the characteristic Zn^{2+}/Zn^0 and $Fe^{3+/}Fe^0$ conversion reactions. Notably, the CV curves retain nearly identical morphologies despite increasing the scan rates, suggesting the enhanced structural stability and mechanical robustness of all three electrodes. Furthermore, using the established matrix-based kinetic equations, the capacitive- and diffusion-controlled contributions are separated to quantify the relative charge-storage mechanisms at each scan rate.[66–68] In detail, across all five scan rates, the pseudocapacitive contribution is dominant over the diffusion-controlled process for all samples. These results suggest that at high scan rates, the electrochemical reactions become kinetically favored at the surface or near-surface regions, as the limited diffusion time restricts Li^+ penetration into the bulk.[69,70] Consequently, the system shifts away from bulk-phase conversion behavior and toward a surface-controlled redox mechanism. Another striking point is that this behavior can be attributed to the nanoscale particle size, which considerably increases the specific surface area and generates a high density of electroactive interfaces, thereby promoting both conventional conversion reactions and fast pseudocapacitive surface processes.[64,71] Furthermore, the combined effects of a small particle size and high crystallinity facilitate efficient electron transport and minimize mechanical stress during lithiation/delithiation, maintaining a highly reversible pseudocapacitive response even at elevated scan rates.[71,72] ZFO_pH 11 exhibits the highest pseudocapacitive fraction, reaching 92.56% at 1.2 mV s^{-1}, even at elevated scan rates (Fig. 9e). This strong pseudocapacitive response is consistent with its nanoscale morphology, as confirmed by TEM (Fig. S3), which provides abundant electroactive sites for rapid surface reactions. As surface-controlled redox reactions dominate, ZFO_pH 11 can effectively utilize a larger fraction of its electroactive surface during lithiation, which directly contributes to both its high-rate capability and superior charge capacity (Fig. 8b). Conversely, the ZFO_pH 12 electrode exhibits inferior electrochemical performance relative to the other two samples, suggesting that the elevated pH conditions likely promote excessive crystallization or the formation of competing hydroxo complexes, thereby reducing the effective Zn content, which is consistent with the CV analysis. Collectively, these results confirm that ZFO_pH 11 possesses a structurally stable framework and a synergistic combination of optimal particle size and robust crystallinity. This combination facilitates the formation of abundant electroactive sites for redox reactions while effectively mitigating the internal stress during lithiation and delithiation.

Galvanostatic intermittent titration technique (GITT) profiles of the ZFO electrodes during the discharge process are

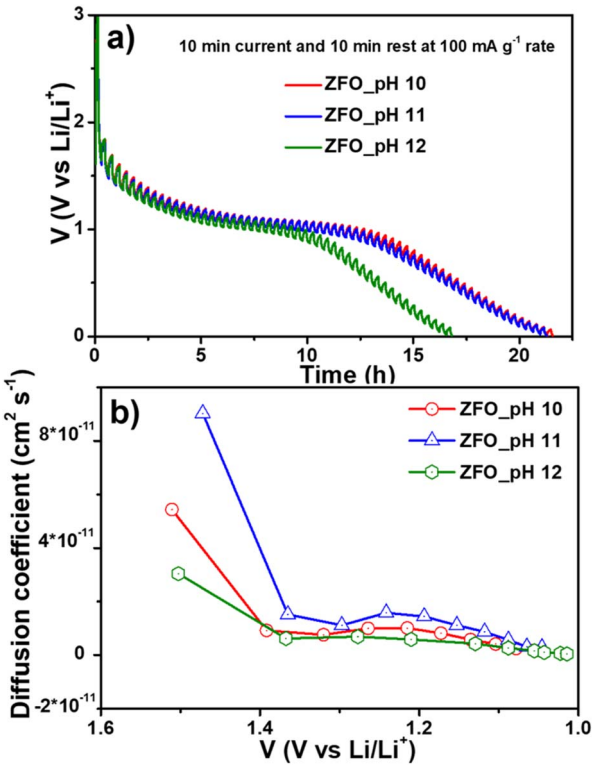

Fig. 10 (a) GITT profiles of the ZFO electrodes during discharge and (b) diffusion coefficients (D) of the ZFO electrodes at different discharge voltages.

presented in Fig. 10a. The corresponding Li^+ diffusion coefficients (D) as a function of discharge voltage are presented in Fig. 10b. The calculated D values of the ZFO electrodes were in the range of 1.7×10^{-12}–5.4×10^{-11} cm^2 s^{-1} for the ZFO_pH 10 electrode, 2.9×10^{-12}–9×10^{-11} cm^2 s^{-1} for the ZFO_pH 11 electrode, and 0.4×10^{-12}–3.1×10^{-11} cm^2 s^{-1} for the ZFO_pH 12 electrode, indicating distinct Li^+ diffusion behaviors among the three samples. Notably, the ZFO_pH 11 electrode exhibits the highest Li^+ diffusion coefficients over most of the investigated voltage range, suggesting more favorable Li^+ transport kinetics. In comparison, the ZFO_pH 10 electrode shows moderate D values, while the ZFO_pH 12 electrode displays relatively lower diffusion coefficients, indicative of slower Li^+ diffusion behavior. These differences in Li^+ diffusion kinetics are in good agreement with the electrochemical performance trends observed in cycling stability, rate capability, CV analysis, and EIS measurements, highlighting the critical role of Li^+ transport properties in determining the overall electrochemical performance of the ZFO electrodes.

4 Conclusions

The $ZnFe_2O_4$ spinel electrode was synthesized *via* a co-precipitation method with a precise pH adjustment at three distinct values and subsequently calcined at 750 °C. In detail, XRD, SEM, TEM, and EDS analyses reveal that pH strongly affects the particle size, crystallinity, and Zn/Fe stoichiometry, which, in turn, governs the electrochemical performance of the $ZnFe_2O_4$ spinel electrode. A noticeable deviation from the ideal Zn/Fe stoichiometry (from EDS) suggests partial Zn loss, which contributes to the deterioration of the cycling performance. In contrast, pH 11 yields particles with optimal size and crystallinity; the ZFO_pH 11 sample retains a capacity of approximately 910.84 mAh g^{-1} after 60 cycles at 0.1 A g^{-1}, corresponding to an excellent capacity retention of approximately 91.8%. Notably, ZFO_pH 11 also demonstrates the highest pseudocapacitive contribution, reaching 92.56% over the entire range of scan rates, thereby indicating that fast surface-dominated redox reactions play a crucial role in charge storage. In addition, the lowest charge-transfer resistance among the three samples further confirms its enhanced electronic conductivity and rapid reaction kinetics, which result in its superior rate capability and long-term cycling stability. Overall, these findings demonstrate that pH regulation is an effective strategy for tailoring particle size, crystallinity, and stoichiometry, thereby optimizing $ZnFe_2O_4$ as a high-performance anode material for LIBs.

Author contributions

To Giang Tran: formal analysis, investigation; Thi My Dung Ngo: methodology; Anh Huy Phan: formal analysis; Hai Dang Ngo: resources; Ngoc Trung Tran: data curation; Hieu Trung Bui: investigation; Tuan Loi Nguyen: writing – original draft; Tran Thi Kieu Ngan: visualization; Il Tae Kim: writing – original draft; Quang Hung Nguyen: conceptualization, funding acquisition, supervision, writing – review, and editing.

Conflicts of interest

There are no conflicts to declare.

Data availability

Additional supporting data are provided in the supplementary information (SI) accompanying this article. Supplementary information is available. See DOI: https://doi.org/10.1039/d5ra10094a.

Acknowledgements

This work was funded by the National Foundation for Science and Technology Development (NAFOSTED) of Vietnam through Grant No. 103.02-2023.20. This work was also supported by the Gachon University research fund of 2025 (202503110001).

References

1 C. Zhong, S. Weng, Z. Wang, C. Zhan and X. Wang, *Nano Energy*, 2023, **117**, 108894.
2 C. Yang, X. Zhang, J. Li, J. Ma, L. Xu, J. Yang, S. Liu, S. Fang, Y. Li, X. Sun, X. Yang, F. Pan, J. Lu and D. Yu, *Electrochim. Acta*, 2020, **346**, 136244.
3 K. Roy, A. Banerjee and S. Ogale, *ACS Appl. Mater. Interfaces*, 2022, **14**, 20326–20348.

4 W. Xu, C. Welty, M. R. Peterson, J. A. Read and N. P. Stadie, *J. Electrochem. Soc.*, 2022, **169**, 010531.
5 P. Zhang, T. Yuan, Y. Pang, C. Peng, J. Yang, Z.-F. Ma and S. Zheng, *J. Electrochem. Soc.*, 2019, **166**, A5489.
6 Y. Zhao, Y. Fu, Y. Meng, Z. Wang, J. Liu and X. Gong, *Chem. Eng. J.*, 2024, **480**, 148047.
7 J. R. Szczech and S. Jin, *Energy Environ. Sci.*, 2011, **4**, 56–72.
8 S. Goriparti, E. Miele, F. De Angelis, E. Di Fabrizio, R. P. Zaccaria and C. Capiglia, *J. Power Sources*, 2014, **257**, 421–443.
9 M. K. Kim, B. Y. Jang, J. S. Lee, J. S. Kim and S. Nahm, *J. Power Sources*, 2013, **244**, 115–121.
10 N. Ding, J. Xu, Y. Yao, G. Wegner, I. Lieberwirth and C. Chen, *J. Power Sources*, 2009, **192**, 644–651.
11 L. Hu, H. Zhong, X. Zheng, Y. Huang, P. Zhang and Q. Chen, *Sci. Rep.*, 2012, **2**, 986.
12 M. Bohra, V. Alman and R. Arras, *Nanomaterials*, 2021, **11**, 1286.
13 A. Varzi, D. Bresser, J. von Zamory, F. Müller and S. Passerini, *Adv. Energy Mater.*, 2014, **4**, 1400054.
14 Q. Su, S. Wang, L. Yao, H. Li, G. Du, H. Ye and Y. Fang, *Sci. Rep.*, 2016, **6**, 28197.
15 D. Z. C. Martin, R. Boston, B. A. Adedayo, R. I. Smith, P. J. Baker, M. Diaz-Lopez, V. Celorrio and N. Reeves-McLaren, *Phys. Chem. Chem. Phys.*, 2025, **27**, 21784–21799.
16 R. Hendriks, D. M. Cunha, D. P. Singh and M. Huijben, *ACS Appl. Energy Mater.*, 2018, **1**, 7046–7051.
17 D. Z. Martin, A. R. Haworth, W. L. Schmidt, P. J. Baker, R. Boston, K. E. Johnston and N. Reeves-McLaren, *Phys. Chem. Chem. Phys.*, 2019, **21**, 23111–23118.
18 Y. Huang, Y. Dong, S. Li, J. Lee, C. Wang, Z. Zhu, W. Xue, Y. Li and J. Li, *Adv. Energy Mater.*, 2021, **11**, 2000997.
19 Z. Chchiyai, O. El Ghali, A. Lahmar, J. Alami and B. Manoun, *Molecules*, 2023, **28**, 7010.
20 M.-S. Park, J. Kim, K. J. Kim, J.-W. Lee, J. H. Kim and Y. Yamauchi, *Phys. Chem. Chem. Phys.*, 2015, **17**, 30963–30977.
21 R. Wang, X. Chen, Z. Huang, J. Yang, F. Liu, M. Chu, T. Liu, C. Wang, W. Zhu, S. Li, S. Li, J. Zheng, J. Chen, L. He, L. Jin, F. Pan and Y. Xiao, *Nat. Commun.*, 2021, **12**, 3085.
22 Q. Q. Viet Thieu, W. G. Kidanu, H. D. Nguyen, T. L. Thi Nguyen, M. L. Phung Le, V. H. Nguyen, D. Q. Nguyen, N. T. Tran, X. V. Nguyen, I. T. Kim and T. L. Nguyen, *Ceram. Int.*, 2022, **48**, 31470–31477.
23 D. Bresser, S. Passerini and B. Scrosati, *Energy Environ. Sci.*, 2016, **9**, 3348–3367.
24 H. Yue, T. Du, Q. Wang, Z. Shi, H. Dong, Z. Cao, Y. Qiao, Y. Yin, R. Xing and S. Yang, *ACS Omega*, 2018, **3**, 2699–2705.
25 H. Jia, R. Kloepsch, X. He, M. Evertz, S. Nowak, J. Li, M. Winter and T. Placke, *Acta Chim. Slov.*, 2016, **63**, 470–483.
26 B. Yao, Z. Wang, C. Ding, M. Feng, Z. Li and Y. Huang, *Electron. Mater. Lett.*, 2023, **19**, 29–37.
27 S. B. Somvanshi, M. V. Khedkar, P. B. Kharat and K. M. Jadhav, *Ceram. Int.*, 2020, **46**, 8640–8650.
28 P. Ren, J. Zhang and H. Deng, *J. Wuhan Univ. Technol., Mater. Sci. Ed.*, 2009, **24**, 927–930.
29 A. Moezzi, P.-S. Lee, A. M. McDonagh and M. B. Cortie, *J. Solid State Chem.*, 2020, **286**, 121311.
30 R. A. Rahmayeni, Y. Stiadi, N. Jamarun and A. S. Emriadi, *J. Mater. Environ. Sci.*, 2017, **8**, 1634–1643.
31 J. Zhu, Y. Zhu, Z. Chen, S. Wu, X. Fang and Y. Yao, *Int. J. Environ. Res. Public Health*, 2022, **19**, 10710.
32 T. Dippong, A. M. Savolszki-Madaras, R. M. Reiz, I. Petean and O. Cadar, *Nanomaterials*, 2025, **15**, 1644.
33 Nitika, A. Rana and V. Kumar, *Appl. Phys. A*, 2021, **127**, 609.
34 J. Yao, Y. Zhang, J. Yan, H. Bin, Y. Li and S. Xiao, *Mater. Res. Bull.*, 2018, **104**, 188–193.
35 Z. Wang, H. Zhu, L. Ai, J. Ding, P. Zhu, Z. Li, B. Li, H. Jiang, F. Yu, X. Duan and H. Jiang, *Nanomaterials*, 2021, **11**, 1122.
36 H. Hwang, H. Shin and W.-J. Lee, *Sci. Rep.*, 2017, **7**, 46378.
37 M. A. Ait Kerroum, A. Essyed, C. Iacovita, W. Baaziz, D. Ihiawakrim, O. Mounkachi, M. Hamedoun, A. Benyoussef, M. Benaissa and O. Ersen, *J. Magn. Magn. Mater.*, 2019, **478**, 239–246.
38 X. Guo, X. Lu, X. Fang, Y. Mao, Z. Wang, L. Chen, X. Xu, H. Yang and Y. Liu, *Electrochem. Commun.*, 2010, **12**, 847–850.
39 M. Maghsoodi, C. Jacquin, B. Teychené, G. Lesage and S. D. Snow, *Langmuir*, 2023, **39**, 3752–3761.
40 B. Ajitha, Y. Ashok Kumar Reddy and P. Sreedhara Reddy, *Powder Technol.*, 2015, **269**, 110–117.
41 M. Aadil, A. G. Taki, S. Zulfiqar, A. Rahman, M. Shahid, M. F. Warsi, Z. Ahmad, A. A. Alothman and S. Mohammad, *RSC Adv.*, 2023, **13**, 28063–28075.
42 K. R. Tallman, P. J. West, S. Yan, S. Yao, C. D. Quilty, F. Wang, A. C. Marschilok, D. C. Bock, K. J. Takeuchi and E. S. Takeuchi, *Nanotechnology*, 2021, **32**, 375403.
43 Y. Tian, Z. Chen, W. Tang, Z. Yang, W. Zhang, S. Li, K. Wang, Y. Sun, Q. Xia and B. Guo, *J. Alloys Compd.*, 2017, **720**, 376–382.
44 H. Cao, X. Xiao, X. Wang, J. Liu and P. Si, *Electrochim. Acta*, 2020, **330**, 135260.
45 J. Yao, J. Yan, Y. Huang, Y. Li, S. Xiao and J. Xiao, *Front. Chem.*, 2018, **6**, 442.
46 S. A. Chambers, T. C. Droubay, T. C. Kaspar, I. H. Nayyar, M. E. McBriarty, S. M. Heald, D. J. Keavney, M. E. Bowden and P. V. Sushko, *Adv. Funct. Mater.*, 2017, **27**, 1605040.
47 A. U. Rehman, M. Atif, M. Younas, T. Rafique, H. Wahab, A. Ul-Hamid, N. Iqbal, Z. Ali, W. Khalid and M. Nadeem, *RSC Adv.*, 2022, **12**, 12344–12354.
48 Y. Ding, Y. Yang and H. Shao, *Electrochim. Acta*, 2011, **56**, 9433–9438.
49 Y. Gao, L. Yin, S. J. Kim, H. Yang, I. Jeon, J.-P. Kim, S. Y. Jeong, H. W. Lee and C. R. Cho, *Electrochim. Acta*, 2019, **296**, 565–574.
50 H. Xu, X. Chen, L. Chen, L. E. Li, L. Xu, J. Yang and Y. Qian, *Int. J. Electrochem. Sci.*, 2012, **7**, 7976–7983.
51 T. N. Vo, T.-A. Nguyen, D. M. K. Nguyen, M. T. Nguyen, T. L. T. Nguyen, M. L. P. Le, V. H. Nguyen, V. M. Tran, D. Q. Nguyen, I. T. Kim and T. L. Nguyen, *Ceram. Int.*, 2023, **49**, 38824–38834.
52 S. J. An, J. Li, C. Daniel, D. Mohanty, S. Nagpure and D. L. Wood, *Carbon*, 2016, **105**, 52–76.

53 C.-J. Huang, B. Thirumalraj, H.-C. Tao, K. N. Shitaw, H. Sutiono, T. T. Hagos, T. T. Beyene, L.-M. Kuo, C.-C. Wang, S.-H. Wu, W.-N. Su and B. J. Hwang, *Nat. Commun.*, 2021, **12**, 1452.
54 B. Zhu, G. Liu, G. Lv, Y. Mu, Y. Zhao, Y. Wang, X. Li, P. Yao, Y. Deng, Y. Cui and J. Zhu, *Sci. Adv.*, 2019, **5**, eaax0651.
55 Y. Zhou, M. Su, X. Yu, Y. Zhang, J.-G. Wang, X. Ren, R. Cao, W. Xu, D. R. Baer, Y. Du, O. Borodin, Y. Wang, X.-L. Wang, K. Xu, Z. Xu, C. Wang and Z. Zhu, *Nat. Nanotechnol.*, 2020, **15**, 224–230.
56 A. T. Nguyen, V. D. Phung, V. O. Mittova, H. D. Ngo, T. N. Vo, M. L. L. Thi, V. H. Nguyen, I. Y. Mittova, M. L. P. Le, Y. N. Ahn, I. T. Kim and T. L. Nguyen, *Scr. Mater.*, 2022, **207**, 114259.
57 Y. Lou, J. Liang, Y. Peng and J. Chen, *Phys. Chem. Chem. Phys.*, 2015, **17**, 8885–8893.
58 M. Kundu, G. Karunakaran, N. Van Minh and D. Kuznetsov, *J. Cluster Sci.*, 2017, **28**, 1285–1293.
59 A. T. Nguyen, T.-A. Nguyen, V. O. Mittova, H. D. Ngo, M. L. P. Le, D. Q. Nguyen, I. Y. Mittova, V. H. Nguyen, S. Hiroshi, H. T. Bui and T. L. Nguyen, *J. Mater. Sci.: Mater. Electron.*, 2022, **33**, 19082–19091.
60 H. Li, H.-Z. Wu and G.-X. Xiao, *Powder Technol.*, 2010, **198**, 157–166.
61 R. A. Reichle, K. G. McCurdy and L. G. Hepler, *Can. J. Chem.*, 1975, **53**, 3841–3845.
62 A. Mukhopadhyay and B. W. Sheldon, *Prog. Mater. Sci.*, 2014, **63**, 58–116.
63 F. Pistorio, D. Clerici, F. Mocera and A. Somà, *Energies*, 2022, **15**, 9168.
64 F. Zhu, X. Peng, X. Hu and L. Kong, *J. Hazard. Mater.*, 2022, **438**, 129484.
65 S. Motahari, M. R. Malayeri and M. Manteghian, *RSC Adv.*, 2025, **15**, 47766–47789.
66 M. Opitz, J. Yue, J. Wallauer, B. Smarsly and B. Roling, *Electrochim. Acta*, 2015, **168**, 125–132.
67 C. Costentin, T. R. Porter and J.-M. Savéant, *ACS Appl. Mater. Interfaces*, 2017, **9**, 8649–8658.
68 G. Z. Chen, *Prog. Nat. Sci.:Mater. Int.*, 2021, **31**, 792–800.
69 V. Augustyn, J. Come, M. A. Lowe, J. W. Kim, P.-L. Taberna, S. H. Tolbert, H. D. Abruña, P. Simon and B. Dunn, *Nat. Mater.*, 2013, **12**, 518–522.
70 X. Han, Q. Meng, X. Wan, B. Sun, Y. Zhang, B. Shen, J. Gao, Y. Ma, P. Zuo, S. Lou and G. Yin, *Nano Energy*, 2021, **81**, 105635.
71 J. Wang, J. Polleux, J. Lim and B. Dunn, *J. Phys. Chem. C*, 2007, **111**, 14925–14931.
72 Y. Son, J. Ma, N. Kim, T. Lee, Y. Lee, J. Sung, S.-H. Choi, G. Nam, H. Cho, Y. Yoo and J. Cho, *Adv. Energy Mater.*, 2019, **9**, 1803480.